Optical properties of $GaAs/Al_{1-x}Ga_xAs$ quantum wells subjected to large in-plane uniaxial stress

G. Rau, A. R. Glanfield, P. C. Klipstein, and N. F. Johnson
Clarendon Laboratory, Physics Department, Oxford University, Parks Road, Oxford OX1 3PU, United Kingdom

G. W. Smith
DERA, St. Andrews Road, Malvern, Worcestershire WR14 3PS, United Kingdom

(Received 21 December 1998)

A comprehensive theoretical study of the effects of in-plane uniaxial stress on the excitonic absorption spectra of $GaAs/Al_xGa_{1-x}As$ quantum wells is presented. In particular, stress is used to investigate optical features of excitonic mixing effects. State-of-the-art calculations of realistic excitonic absorption spectra under stress are performed that take valence-band mixing *and* the stress-induced anisotropy of the band structure into account. Two important aspects of in-plane uniaxial stress are identified each of which affects exciton mixing in a different way. On the one hand, the natural quantization direction gets rotated by stress from the confinement direction to the stress direction. This leads to a marked polarization dependence of the absorption spectrum, which can be explained within a simple model of single-particle zone-center states. On the other hand, uniaxial stress also allows the energy alignments of the valence states to be varied substantially. Thereby it is possible to influence the $\mathbf{k}\cdot\mathbf{p}$-related exciton mixing considerably, in particular between the lowest 1*s* light-hole exciton and the *p* continuum of the second heavy-hole exciton. This leads to the formation of doublet structures that reveal strong anticrossing behavior and have peculiar properties, which are best described within the framework of the Fano-Anderson model. Excellent agreement was achieved up to large stress values between our theoretical results and our experimental photoreflectance and photoluminescence results, with respect to the polarization dependence of the transition intensities and the stress dependence of the exciton energies. This clearly demonstrates the high accuracy of the calculations and provides conclusive evidence for the strong mixing effects that stress can cause. [S0163-1829(99)04424-0]

I. INTRODUCTION

Even since the advent of layered semiconductor structures, one of the main research interests has been the study of the optical properties of semiconductor quantum wells (QW's). Not only have the optical properties turned out to be of significant use for technological applications, but they also provide important information about the fundamental behavior of electronic properties in an environment of reduced dimensionality. In nominally undoped structures, the optical properties near the fundamental band gap are dominated by excitonic excitations, which in QW's often are strongly mixed.[1–13] There are two principal causes of exciton mixing, the three-dimensional nature of the Coulomb potential and valence-band mixing. This valence-band mixing will provide the main focus of the present work.

A common approach to investigating exciton mixing is to analyze how the excitonic spectrum responds to a change of external perturbation, using optical spectroscopy techniques. So far predominantly external fields, such as magnetic or electric fields, have been used as perturbations.[7,10,14–25] The problem, however, with both electric and magnetic fields is that they mainly affect the exciton itself, i.e., the hydrogenic system, but have a lesser effect on the mixing between different excitons. A more powerful method of specifically changing the mixing between valence subbands and hence excitons in a precisely controllable and reproducible manner is to apply in-plane uniaxial stress. With stress applied, it is possible to change the positions of heavy-hole (HH) and light-hole (LH) energy levels relative to each other. Hence stress tends to modify the relative coupling strength between the various excitons, and accordingly the degree of mixing, but not the absolute coupling strength. Due to this particular property of uniaxial stress, we were able to show theoretically in a previous paper[12] that the strong $\mathbf{k}\cdot\mathbf{p}$ coupling between LH1 and HH2 can lead to the formation of a distinct doublet structure when LH1-CE1(1*s*) is shifted by uniaxial stress towards the onset of the HH2-CE1(*p*) continuum. Since that doublet structure can be best understood within the framework of the Fano-Anderson model, we will refer to it as a ''Fano doublet.''

In our work on Fano doublets we neglected, however, another aspect about in-plane uniaxial stress, which is that uniaxial stress applied perpendicular to the growth direction reduces the symmetry of the QW from tetragonal to orthorhombic. This couples valence states even at the zone center and as a consequence renders the valence-subband structure anisotropic. In a general analysis of the stress-induced mixing effects in excitonic spectra, it is, therefore, necessary to take not only the valence-band mixing but also the anisotropic band structure into account. Thus, the purpose of this paper is to present a realistic model for the theoretical description of excitons in a QW under in-plane uniaxial stress that incorporates all aspects of uniaxial stress. This allows us to discuss in detail the various effects that uniaxial stress has on the optical properties of a semiconductor QW. For simplicity, we will restrict ourselves to $GaAs/Al_xGa_{1-x}As$ QW's that are grown along the [001] direction and hence to stress that is applied along the [100] direction.

Although it is not difficult from a conceptual point of

view to describe excitons theoretically, it is nevertheless a formidable task to obtain numerical solutions for a realistic model of excitons inside a semiconductor QW. For the past 18 years or so QW excitons, therefore, have continued to challenge theoreticians and have led to an enormous wealth of contributions in the literature,[1–11,18,19,21–24,26–57] where the list of references is by no means exhaustive. A recent and more detailed review is given, for example, by Winkler.[11] Common to all these works is that they use the envelope-function approximation combined with linear response theory as a framework for their investigations. But within that framework many different modes of varying degrees of sophistication and refinement have been suggested. But to our knowledge a model that incorporates *both* valence-band mixing *and* the anisotropy of the valence-band structure is still missing. Bauer and Ando included band warping in their calculations,[7] but since they adopted a variational approach, they neglected the important role that the exciton continuum plays in exciton mixing.[4–6] Consequently, their model is not suitable to obtain detailed information about higher excited states in absorption spectra at elevated stress values. Broido and Yang,[9] on the other hand, presented a full valence-band-mixing model that includes uniaxial stress. These authors, however, averaged over the anisotropic band structure, in order to simplify the numerical complexity, and this way effectively restored axial symmetry. To include the stress-induced anisotropy, we extend the model by Chao and Chuang, who developed a state-of-the-art model within the axial approximation that rigorously incorporates valence-band mixing.[10] One of the main challenges about going beyond the axial approximation is to circumvent the limitations that are imposed by the computational resources with respect to storage capacity and speed. We, therefore, also present an efficient and optimized algorithm with which it is possible to obtain numerical solutions for the exciton equation even on an ordinary PC within a few hours.

In addition to the theoretical analysis, we also measured both photoluminescence (PL) and photoreflectance (PR) spectra of a 100 Å GaAs/$Al_{0.2}Ga_{0.8}As$ QW for in-plane uniaxial stress values up to about 10 kbar. This is twice the stress range previously reported in the literature for similar samples[58–66] and hence we were able to resolve stress-induced mixing effects in a particularly pronounced way. Thus, we found not only clear evidence for the formation of Fano doublets, but also managed to detect a strong polarization dependence of the oscillator strength of both ground and higher excited states within the QW plane, which is in excellent agreement with our calculations.

This paper is organized as follows. In Sec. II we first analyze how in-plane uniaxial stress affects the valence-subband structure in GaAs/$Al_xGa_{1-x}As$ QW's, in particular with respect to anisotropic dispersion relations. In the second part of Sec. II we will then give a detailed description of our theoretical model for anisotropic excitons and fundamental absorption at finite stress, while in the third part we will demonstrate how the computational difficulties of obtaining numerical results can be overcome. In Sec. III, we briefly review our experimental technique to measure PL and PR spectra of a 100 Å GaAs/$Al_{0.2}Ga_{0.8}As$ QW under uniaxial stress. Finally, in Sec. IV we discuss our numerical results and compare them with our experimental results. Our conclusions are presented in Sec. V.

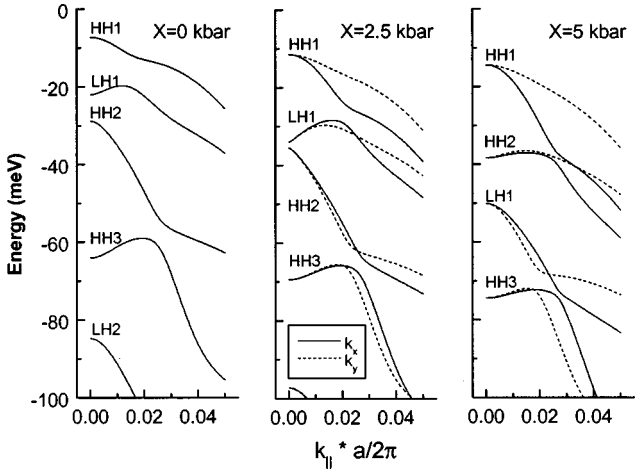

FIG. 1. Valence subband dispersions parallel (solid lines) and perpendicular (dashed lines) to the [100] stress direction for three different stress values in a 100 Å GaAs/$Al_{0.3}Ga_{0.7}As$ QW.

II. THEORY

A. Single-particle picture

In order to understand how in-plane uniaxial stress affects the excitonic absorption spectra of GaAs/$Al_xGa_{1-x}As$ QW's, it is instructive to analyze stress effects in a single-particle picture first. Hence in this subsection we look at how stress modifies the valence-subband structure of GaAs/$Al_xGa_{1-x}As$ QW. In particular, this analysis will give a clear indication as to how the stress-induced anisotropy of the valence subbands can be included in the full-band-mixing model for excitonic calculations presented in the next subsection.

Figure 1 presents the energy dispersions of the first four valence subbands of a 100 Å GaAs/$Al_{0.3}Ga_{0.7}As$ QW for three different stress values, which were calculated using the subband $\mathbf{k}\cdot\mathbf{p}$ method.[1,9,67] The subband $\mathbf{k}\cdot\mathbf{p}$ method is a variational approach where the envelope functions at finite in-plane $\mathbf{k}_{\|}$ values are expanded in terms of a set of zone-center states. The continuum above the QW is included by putting it symmetrically inside an infinite QW of much larger width. The wave vectors are shown in units of $2\pi/a$ in Fig. 1, where a is the lattice constant of GaAs. At zero stress the subbands clearly reveal strong nonparabolic dispersions. Particularly striking is the electronlike curvature of the LH1 subband[68] out to about $0.015(2\pi/a)$. Its origin can be easily understood in terms of two competing mixing effects.[69,70] At small $k_{\|}$ values, LH1 and HH2 repel each other strongly due to an off-diagonal matrix element of the Luttinger-Kohn Hamiltonian that is linear in $k_{\|}$. Consequently, LH1 is bent upwards. At the same time, HH2 is bent further downwards resulting in a decreased effective mass near the zone center. As $k_{\|}$ increases, LH1 approaches HH1, which is coupled to LH1 via an off-diagonal matrix element of the Luttinger-Kohn Hamiltonian that is quadratic in $k_{\|}$. This leads to an anticrossing between these two states and LH1 is bent downwards again. This electronlike dispersion is not unique, however; HH3, for example, reveals the same type of dispersion, which originates from the same type of mechanism as in the case of LH1, except that this time HH3 is repelled by LH2.

Under compressive in-plane uniaxial stress, LH1 is shifted towards HH2 and the relative strength of the coupling between LH1 and HH2 increases. This leads to an enhancement of the above-described effect, i.e., the electronlike dispersion becomes more pronounced and the effective mass of HH2 decreases even further. When the zone-center states of LH1 and HH2 cross at 2.5 kbar, the repulsion reaches a maximum. At this point LH1 and HH2 are strongly mixed with each other. In fact, it turns out that because of the strong coupling between LH1 and HH2, the LH1 subband consists of almost equal amounts of LH1 and HH2 zone-center states for $k_{\|}$ values as large as $2\langle k\rangle_{1s}$, where $\langle k\rangle_{1s}$ refers to the momentum expectation value of the excitonic ground state. This suggests that the excitons attached to these subbands will have a strongly mixed character, too, and hence will show features of an anticrossing behavior, which is precisely what is found in excitonic absorption spectra further below. If the stress is increased even further, LH1 is shifted beyond HH2 and the repulsion between these two subbands weakens again. More importantly, however, HH2 now has an electronlike dispersion while LH1 is approximately parabolic for small $k_{\|}$ values, so in some sense they have swapped their respective characteristic features.

Besides modifying the $\mathbf{k}\cdot\mathbf{p}$ related valence-band-mixing effects, in-plane uniaxial stress also reduces the symmetry of the QW from tetragonal to orthorhombic, which leads to strong mixing between zone-center valence states. Under these circumstances the valence-subband dispersions become strongly anisotropic at elevated stress.[41,71] This can be seen in Fig. 1, which shows the valence-subband dispersions for two directions in $\mathbf{k}$ space: k_x (solid line), which coincides with the stress direction, and k_y (dashed line). The complete anisotropic solutions, however, are not suitable for excitonic calculations, since in this case the Hilbert space of the exciton, and hence the matrix representation of the excitonic Hamiltonian, becomes too large for numerical calculations to still be manageable. It is, therefore, crucial to derive approximate solutions for the anisotropic valence subbands that are simple enough to be included in the excitonic calculations, yet still capture the essence of the stress-induced anisotropy. The best way to achieve this is to expand the solutions of the anisotropic Hamiltonian, i.e., eigenstates and eigenenergies, in terms of simple harmonics. Since in-plane uniaxial stress reduces the symmetry of the QW from tetragonal to orthorhombic, both the eigenenergies and eigenstates have a periodicity of π. Thus the eigenenergies of the valence subbands $E_m(\mathbf{k}_{\|})$ can be expanded in the following way:

$$E_m^h(\mathbf{k}_{\|}) = \sum_{l=0,\pm 2,\ldots} E_m^{hl}(k_{\|}) e^{il\theta}, \tag{1}$$

while the hole envelope functions according to Zhu[39] become

$$g_{m\nu}(\mathbf{k}_{\|}, z) = e^{-i\nu\theta} \sum_{l=0,\pm 2,\ldots} g_{m\nu}^{l}(k_{\|}, z) e^{il\theta}. \tag{2}$$

Approximate solutions can now be conveniently obtained by cutting off higher-order terms in the expansion. The crudest approximation includes the anisotropy only in the lowest order, i.e., it keeps terms only up to $l=\pm 2$. To assess the validity of this approximation, contour plots of the first two valence subbands of a 100 Å GaAs/$Al_{0.3}Ga_{0.7}$As QW at 5 kbar (cf. Fig. 1), which were obtained from the full calculations (solid lines), are compared in Fig. 2 with the corresponding approximate solutions (dashed lines) derived from the simplified expression of the anisotropic subband energy:

$$\tilde{E}_m^h(k_{\|}, \theta) = E_m^{h0}(k_{\|}) + 2E_m^{h2}(k_{\|})\cos(2\theta). \tag{3}$$

The overall agreement in Fig. 2 is excellent; even in the region where the contour lines show strong deviations from the generally prevalent elliptical shape, the approximate solutions accurately reproduce all main features of the subband structure. This provides convincing evidence that it is indeed justified to keep only the zeroth-order (i.e., isotropic) and the first-order (i.e., the first nonisotropic) term in the expansion.

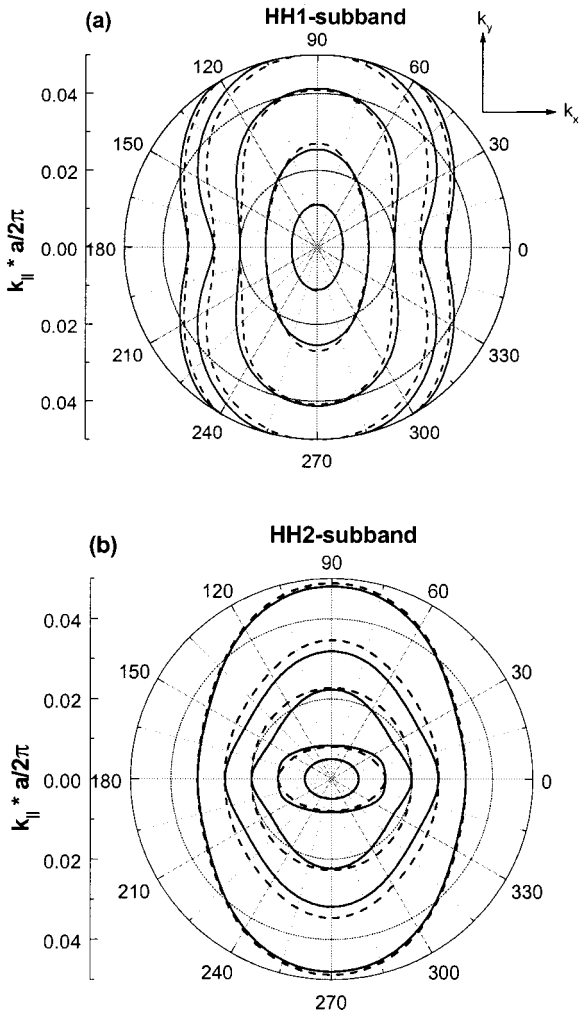

FIG. 2. Contour plots of the first two confined valence subbands in a 100 Å GaAs/$Al_{0.3}Ga_{0.7}$As QW at 5 kbar of compressive in-plane uniaxial stress along the [100] direction. The solid lines represent the exact results whereas the dashed lines represent the approximate results using the Fourier expansion method.

B. Exciton theory beyond the axial approximation

Our excitonic calculations are based on a generalization of the full-band-mixing model by Chao and Chuang,[10] which is a state-of-the-art model that rigorously incorporates valence-band mixing within the Γ_8 subspace. The conduc-

tion band, on the other hand, is assumed to be parabolic. Furthermore, the exchange interaction between electrons and holes[60] and the difference in dielectric constants between well and barrier materials[44–46] are neglected. Since Chao and Chuang only solved the exciton equation within the axial approximation, the purpose of this subsection is to demonstrate how their model can be extended to include the stress-induced anisotropy approximately.

Within the framework of the effective-mass theory and the envelope-function scheme, excitons can be described by the following two-particle Hamiltonian (SI units):

$$H^{\mathrm{ex}}_{\sigma\nu\sigma'\nu'}=H^{e}_{\sigma\sigma'}\delta_{\nu\nu'}+H^{h}_{\nu\nu'}\delta_{\sigma\sigma'}-\frac{e^2}{4\pi\varepsilon\varepsilon_0|\mathbf{r}_e-\mathbf{r}_h|}\,\delta_{\sigma\sigma'}\delta_{\nu\nu'}. \tag{4}$$

$H^{e}_{\sigma\sigma'}$ and $H^{h}_{\nu\nu'}$ are the single-particle kinetic-energy operators of the conduction-band electron and the valence-band hole, respectively, where $\sigma=\pm\frac{1}{2}$ and $\nu=\pm\frac{1}{2},\ \pm\frac{3}{2}$ refer to the corresponding spinor components. The third term in Eq. (4) is the Coulomb interaction, which is diagonal with respect to the spinor components. The exciton wave function accordingly must be an eight-component spinor satisfying the Schrödinger equation

$$\sum_{\sigma'\nu'} H^{\mathrm{ex}}_{\sigma\nu\sigma'\nu'}\Psi^{X}_{\sigma'\nu'}=E_X\Psi^{X}_{\sigma\nu}, \tag{5}$$

where X labels different exciton states. Since both the electron-hole exchange interaction and the nonparabolicity of the conduction band are neglected here, $\Psi^{X}_{\sigma\nu}$ is twofold degenerate with respect to the electron spin σ and thus $\Psi^{X}_{\sigma\nu}$ effectively becomes a four-component spinor. For simplicity we will drop the index σ in $\Psi^{X}_{\sigma\nu}$ henceforth. Considering also Kramers' degeneracy for the valence band, each exciton state is thus in general fourfold degenerate.

In order to solve Eq. (5), the exciton wave function is expanded in terms of products of single-particle electron and hole states:

$$\begin{aligned} f_{n\sigma}(\mathbf{k}_{\|e},\mathbf{r}_e)&=(2\pi)^{-1}f_{n\sigma}(\mathbf{k}_{\|e},z_e)e^{(i\mathbf{k}_{\|e}\cdot\rho_e)},\\ g_{m\nu}(\mathbf{k}_{\|h},\mathbf{r}_h)&=(2\pi)^{-1}g_{m\nu}(\mathbf{k}_{\|h},z_h)e^{(i\mathbf{k}_{\|h}\cdot\rho_h)}, \end{aligned} \tag{6}$$

where n and m are the subband indices for the conduction and valence band, respectively, while the vectors $\mathbf{k}_\|$ and ρ refer to two-dimensional vectors in the x-y plane of momentum and real space, respectively. Before constructing the exciton state, it should be remembered that a hole state is the time-reversed version of the corresponding single-particle electron state. Hence the hole envelope function is obtained from the envelope function of the valence state in Eq. (6) by complex conjugation. With this in mind the exciton wave function becomes

$$\begin{aligned} \Psi^{X}_{\nu}(\rho,z_e,z_h)=\sum_{n',m'}\int\frac{d\mathbf{k}'_\|}{(2\pi)^2}\,\phi^{X}_{n'm'}(\mathbf{k}'_\|)e^{i\mathbf{k}_\|\cdot\rho}\\ \times f_{n'\sigma}(\mathbf{k}'_\|,z_e)g^{*}_{m'\nu}(\mathbf{k}'_\|,z_h), \end{aligned} \tag{7}$$

where $\phi^{X}_{n'm'}(\mathbf{k}'_\|)$ denotes the expansion coefficient and is often called the exciton envelope function.

After this preparation it is now straightforward to derive the exciton equation in $\mathbf{k}_\|$ space by inserting Eq. (7) into Eq. (5), multiplying both sides of Eq. (5) with $f^{*}_{n\sigma}(\mathbf{k}_\|,z_e)g_{m\nu}(\mathbf{k}_\|,z_h)e^{-i\mathbf{k}_\|\cdot\rho}$, summing over ν, and integrating over z_e, z_h, and ρ. This yields the following set of coupled integral equations:

$$\begin{aligned} T_{nm}(\mathbf{k}_\|)\phi^{X}_{nm}(\mathbf{k}_\|)+\sum_{n',m'}\int\frac{d\mathbf{k}'_\|}{(2\pi)^2}V_{nmn'm'}(\mathbf{k}_\|,\mathbf{k}'_\|)\phi^{X}_{n'm'}(\mathbf{k}'_\|)\\ =E_X\phi^{X}_{nm}(\mathbf{k}_\|), \end{aligned} \tag{8}$$

which sometimes is also referred to as the Bethe-Salpeter equation.[9,72] In momentum space the kinetic-energy matrix element $T_{nm}(\mathbf{k}_\|)$ is diagonal and reads

$$T_{nm}(\mathbf{k}_\|)=E^{e}_{n}(k_\|)-E^{h}_{m}(\mathbf{k}_\|), \tag{9}$$

where $E^{e}_{n}(k_\|)/E^{h}_{m}(\mathbf{k}_\|)$ are the subband dispersions of the nth/mth confined electron/hole states. While $E^{e}_{n}(k_\|)$ is parabolic in the approximation adopted here, $E^{h}_{m}(\mathbf{k}_\|)$ in general is highly nonparabolic as was discussed in the preceding subsection. Much more complicated than the kinetic-energy matrix element, however, is the Coulomb matrix element $V_{nmn'm'}(\mathbf{k}_\|,\mathbf{k}'_\|)$ which turns out to be of the form

$$\begin{aligned} V_{nmn'm'}(\mathbf{k}_\|,\mathbf{k}'_\|)=-\frac{e^2}{2\varepsilon\varepsilon_0}\frac{1}{q}\int dz_e\int dz_h e^{-q|z_e-z_h|}\\ \times f^{*}_{n\sigma}(\mathbf{k}_\|,z_e)f_{n'\sigma}(\mathbf{k}'_\|,z_e)\\ \times\sum_{\nu}\,g_{m\nu}(\mathbf{k}_\|,z_n)g^{*}_{m'\nu}(\mathbf{k}'_\|,z_h), \end{aligned} \tag{10}$$

where

$$q=|\mathbf{k}_\|-\mathbf{k}'_\||=\sqrt{k_\|^2+k_\|'^2-2k_\|k'_\|\cos(\theta-\theta')}. \tag{11}$$

Finally, within the dipole approximation the oscillator strength for the excitonic state X is defined as

$$\begin{aligned} f^{\xi}_{X}&=\frac{2}{m_0E_X}\left|\sum_{\nu}\,(\xi\cdot\tilde{P}^{\sigma\nu}_{cv})\int dz\,\Psi^{X}_{\nu}(\rho=0,z,z)\right|^2\\ &=\frac{2}{m_0E_X}\left|\sum_{\nu}\,(\xi\cdot\tilde{\mathbf{P}}^{\sigma\nu}_{cv})\sum_{n,m}\int\frac{d\mathbf{k}'_\|}{(2\pi)^2}\phi^{X}_{nm}(\mathbf{k}'_\|)I^{\sigma\nu}_{nm}(\mathbf{k}'_\|)\right|^2, \end{aligned} \tag{12}$$

where

$$I^{\sigma\nu}_{nm}(\mathbf{k}_\|)=\int dz\,f_{n\sigma}(\mathbf{k}_\|,z)g^{*}_{m\nu}(\mathbf{k}_\|,z) \tag{13}$$

is the overlap integral between the conduction and valence subbands. Summation over the electron spin σ is omitted in Eq. (12) due to the twofold degeneracy of the conduction-band states with respect to σ. This, however, means that the momentum matrix element between the conduction- and valence-band Bloch functions needs to be slightly modified to ensure that all allowed transitions are included in Eq. (12):

$$\tilde{\mathbf{P}}^{\sigma\nu}_{cv}=\langle u^{\sigma}_{c}|\mathbf{p}|u^{\nu\cos[(\nu+\sigma)\pi]}_{\nu}\rangle. \tag{14}$$

Once the excitonic oscillator strengths are known, the absorption coefficient can be calculated by summing up the contributions from all excitonic states:

$$\alpha(E)=\frac{\pi e^2\hbar}{2n_r\varepsilon_0 c m_0 L}\sum_X f_X^{\xi}\frac{\frac{\Gamma_X}{2\pi}}{(E-E_X)^2+\left(\frac{\Gamma_X}{2}\right)^2}. \quad (15)$$

Here we have replaced the δ function by a phenomenological Lorentzian broadening. Γ_X is the linewidth of the Lorentzian and is chosen empirically, partially to match the experimental data presented below and partially to match the resolution of the energy spectrum obtained in numerical calculations.

Equation (8) is a two-dimensional integral equation, which in general is very laborious to solve numerically. Thus, in previous works the numerical treatment of the exciton equation was usually tackled by invoking the axial approximation, i.e., by neglecting the warping of the valence band, in which case the two-dimensional integral equation simplifies to a one-dimensional one. In the presence of in-plane uniaxial stress this is no longer possible, however, because of the anisotropic band dispersions induced by stress. To include the effects of stress on excitons at least approximately, it is therefore necessary to go beyond the axial approximation. This means that at finite stress the exciton wave functions need to be written as a linear combination of wave functions with different total angular momenta:

$$\phi_{nm}^{X}(k_\parallel,\theta)=\sum_{s'}\phi_{nm}^{Xs'}(k_\parallel)e^{is'\theta}. \quad (16)$$

Inserting Eq. (16) into Eq. (8), multiplying by $e^{-is\theta}$, and integrating over θ yields the exciton equation

$$\sum_{s'}T_{nm}^{s-s'}(k_\parallel)\phi_{nm}^{Xs'}(k_\parallel)+\sum_{n',m'}\sum_{s'}\int_0^\infty\frac{k_\parallel' dk_\parallel'}{2\pi}V_{nmn'm'}^{ss'}(k_\parallel,k_\parallel')\phi_{n'm'}^{Xs'}(k_\parallel')=E_X\phi_{nm}^{Xs}(k_\parallel), \quad (17)$$

where $T_{nm}^{s'}(k_\parallel)$ and $V_{nmn'm'}^{ss'}(k,k_\parallel')$ are Fourier components of the kinetic energy and Coulomb matrix element, respectively, i.e.,

$$T_{nm}(k_\parallel,\theta)=\sum_{s'}T_{nm}^{s'}(k_\parallel)e^{is'\theta}, \quad (18)$$

$$V_{nmn'm'}(k_\parallel,k_\parallel',\theta,\theta')=\sum_s\sum_{s'}V_{nmn'm'}^{ss'}(k_\parallel,k_\parallel')e^{is\theta}e^{-is'\theta'}. \quad (19)$$

The Fourier components of the Coulomb matrix element can be determined by Fourier expanding the single-particle envelope functions in Eq. (10). Since the conduction-band subspace Γ_6 is isotropic, the angular dependence of the electron envelope functions is simply

$$f_{n\sigma}(\mathbf{k}_\parallel,z_e)=f_n(k_\parallel,z_e)e^{-i\sigma\theta}. \quad (20)$$

Together with the corresponding expression for the hole envelope functions presented in Eq. (2), $V_{nmn'm'}^{ss'}(k_\parallel,k_\parallel')$ can thus be shown to adopt the following form:

$$V_{nmn'm'}^{ss'}(k_\parallel,k_\parallel')=-\frac{e^2}{2\varepsilon\varepsilon_0}\sum_\nu\sum_{l=0,\pm2,\ldots}\times\int dz_e\int dz_h\int_0^{2\pi}\frac{d\Delta\theta}{2\pi}\times\frac{e^{-q|z_e-z_h|}}{q}e^{i[\sigma-\nu-(s-l)]\Delta\theta}f_n^*(k_\parallel,z_e)\times f_{n'}(k_\parallel',z_e)g_{m\nu}^{l}(k_\parallel,z_h)g_{m'\nu}^{l-(s-s')*}(k_\parallel',z_h), \quad (21)$$

while the oscillator strength becomes

$$f_X^{\xi}=\frac{2}{m_0E_X}\left|\sum_\nu(\xi\cdot\tilde{\mathbf{P}}_{cv}^{\sigma\nu})\sum_{n',m'}\sum_s\sum_{l=0,\pm2,\ldots}\times\int_0^\infty\frac{k_\parallel' dk_\parallel'}{2\pi}\phi_{n'm'}^{Xs}(k_\parallel')I_{n'm'}^{\nu l}(k_\parallel')\delta_{s-l,\sigma-\nu}\right|^2, \quad (22)$$

where

$$I_{nm}^{\nu l}(k_\parallel)=\int dz\, f_n(k_\parallel,z)g_{m\nu}^{l*}(k_\parallel,z). \quad (23)$$

In the absence of stress, only the zeroth-order term of $g_{m\nu}^{l}(k_\parallel,z)$ is nonzero, in which case Eqs. (21) and (22) simplify to the corresponding expressions of the axial approximation.[10] Furthermore, from Eq. (21) it can be immediately concluded that the stress-induced anisotropy only couples angular momenta that differ at least by 2, i.e., $\Delta s=s-s'=\pm2$, which follows from the fact that uniaxial stress applied perpendicular to the growth direction only couples different types of holes, i.e., heavy holes with light holes, but not holes of the same kind. In view of this result, the simplest extension of the axial approximation is to consider the coupling between only those four total angular momenta that have nonzero contributions to the oscillator strength under the axial approximations, i.e., $s=\sigma+\frac{3}{2}$, $\sigma+\frac{1}{2}$, $\sigma-\frac{1}{2}$, $\sigma-\frac{3}{2}$. Within that subspace, Eq. (21) becomes block-diagonal, where one block comprises $s=\sigma+\frac{3}{2}$ and $\sigma-\frac{1}{2}$ and the other $s=\sigma+\frac{1}{2}$ and $\sigma-\frac{3}{2}$. Consequently, the final matrix equation is in this case twice the size of the respective axially symmetric matrix equation and hence numerically still feasible. Furthermore, it should be noted that under this approximation only the first nonisotropic Fourier component of the hole envelope function is taken into account. But as was mentioned in the preceding subsection, this already captures the essence of the stress-induced anisotropy. It is, therefore, reasonable to expect that the restriction to those four total angular momenta is adequate.

C. Computational details

A standard procedure for solving integral equations such as the exciton equation (17) is to discretize the integral, i.e., to replace the integral by a finite sum, which turns the inte-

gral equation into a linear matrix equation. Details of this are given in the Appendix. Here we want to comment briefly on the considerable difficulties that one encounters in solving the matrix equation in practice. The difficulties stem mainly from two types of limitations imposed by the computational resources: operational memory and processor speed, both of which set restrictions on the size of the matrices. For that reason, it is necessary to discuss first how large the matrices need to be in order to obtain reliable results, and how these requirements can be made compatible with the available computer power. Second, we will describe a technique that we developed to speed up calculations of the matrix elements significantly.

The size of a matrix is determined by the number of conduction and valence subbands that are included in the expansion of the exciton wave function and, most importantly, the number of k values. In this work we are interested in studying the effects of mixing between the lower valence subbands, i.e., HH1, LH1, HH2, and HH3. Since the measured absorption spectra, which will be used further below for comparison with theoretical results, also resolve higher excited states, i.e., HH2-CE2, both the first and the second confined electron state, CE1 and CE2, need to be included. Hence the only remaining question is how many k values need to be included in the numerical calculations. In order to obtain a smooth absorption spectrum, the number of k values has to be large enough so that the average energy separation of two consecutive exciton states determined from the numerical calculations is much smaller than the linewidth Γ_X of the Lorentzian attached to each exciton state. In practice, it is sufficient to have a Γ_X that is about five times larger than the average exciton separation energy. If ΔE refers to the energy range over which the excitonic spectrum is calculated, i.e., the energy separation between HH1-CE1 and HH2-CE2, then the following relationship serves as a suitable rule of thumb to estimate the minimum number N of k values:

$$N > \frac{5\Delta E}{\Gamma_X}. \tag{24}$$

In a 100 Å GaAs/$Al_{0.3}Ga_{0.7}$As QW, ΔE is about 150 meV, while experimental spectra yield a broadening Γ_X of the order of 4 meV. Hence, according to Eq. (24) at least 190 k values should be used for an accurate comparison between theory and experiment. Hence within the numerical approach outlined above, the minimum dimension of the discretized $n \times n$ Hamiltonian has $n = 2 \times 2 \times 4 \times 190 = 3040$, which is obviously very large. For that reason, coupling between excitons attached to different conduction subbands will be neglected henceforth. For the physical system considered here, this is a justifiable assumption, since the confined electron states are usually far apart due to their light effective mass. In a 100 Å GaAs/$Al_{0.3}Ga_{0.7}$As QW, the energy separation between CE1 and CE2 is 91 meV and thus almost twice as large as the energy separation between HH1 and HH3. Consequently, the higher excited exciton states attached to CE2 are well separated from the corresponding states linked to CE1. This approximation is not valid in general, however. In the presence of an electric field, for example, CE1 and CE2 are typically strongly coupled.

Another problem that needs to be tackled is the calculation of the matrix elements. Equation (21) reveals that the matrix elements of the Coulomb potential are obtained by solving a triple integral, which in general is very time-consuming. The subband $\mathbf{k}\cdot\mathbf{p}$ method employed here is particularly advantageous in this respect. By using the subband $\mathbf{k}\cdot\mathbf{p}$ method, it is possible to carry out the integration over the hole and electron coordinates in Eq. (21) analytically. Hence the triple integral is reduced to a single integral, which is much easier to solve numerically. In the subband $\mathbf{k}\cdot\mathbf{p}$ method, the hole envelope function $g_{m\nu}(\mathbf{k}_\parallel, z_h)$ at finite $\mathbf{k}_\parallel$ value is expanded in terms of zone-center states, i.e.,

$$g_{m\nu}(\mathbf{k}_\parallel, z_h) = \sum_{r'} a^{\nu}_{mr'}(\mathbf{k}_\parallel) g_{r'\nu}(z_h), \tag{25}$$

where the expansion coefficients $a^{\nu}_{mr}(\mathbf{k}_\parallel)$ themselves can be Fourier expanded in analogy with Eq. (2):

$$a^{\nu}_{mr}(k_\parallel, \theta) = e^{-i\nu\theta} \sum_{l'=0,\pm 2} a^{\nu l'}_{mr}(k_\parallel) e^{il'\theta}. \tag{26}$$

Before rewriting Eq. (21) in this basis, the following integral given by Bauer and Ando[7] has to be introduced, since it allows separation of the hole and electron integrals:

$$e^{-q|z_e - z_k|} = \frac{1}{\pi} \int_{-\infty}^{\infty} dt \, \frac{q}{q^2 + t^2} \cos[t(z_e - z_h)]. \tag{27}$$

Inserting now Eqs. (25), (26), and (27) into Eq. (21) thus yields

$$\begin{aligned} V^{ss'}_{nmn'm'}(k_\parallel, k'_\parallel) = & -\frac{e^2}{2\varepsilon\varepsilon_0\pi} \sum_{\nu} \sum_{l=0,\pm 2} \sum_{rr'} \\ & \times a^{\nu l}_{mr}(k_\parallel) a^{\nu[l-(s-s')]*}_{m'r'}(k'_\parallel) \\ & \times \int_0^{2\pi} \frac{d\Delta\theta}{2\pi} I^{\nu}_{nrn'r'}(q) \\ & \times \cos\{[\sigma - \nu - (s-l)]\Delta\theta\}, \end{aligned} \tag{28}$$

where

$$\begin{aligned} I^{\nu}_{nrn'r'}(q) = & \int_{-\infty}^{\infty} dt \, \frac{1}{q^2 + t^2} \int dz_e f^*_n(z_e) f_{n'}(z_e) \cos(tz_e) \\ & \times \int dz_h g_{r\nu}(z_h) g^*_{r'\nu}(z_h) \cos(tz_h) \\ & + \int_{-\infty}^{\infty} dt \, \frac{1}{q^2 + t^2} \int dz_e f^*_n(z_e) f_{n'}(z_e) \sin(tz_e) \\ & \times \int dz_h g_{r\nu}(z_h) g^*_{r'\nu}(z_h) \sin(tz_h). \end{aligned} \tag{29}$$

The crucial point about the integrals in Eq. (29) is that they can be solved analytically due to the simple form of the zone-center states. Deriving the algebraic expression of $I^{\nu}_{nrn'r'}(q)$ is straightforward but nevertheless extremely lengthy. It should be noted that under the assumption con-

sidered here, i.e., no coupling between excitons attached to different conduction subbands, the second term of Eq. (29) is always zero.

The computation time, however, can be lowered even further by taking the following property of $I^{\nu}_{nrn'r'}(q)$ into account. Since $I^{\nu}_{nrn'r'}(q)$ is derived from zone-center states at zero stress, it is independent of the applied stress. The effect of stress and in fact band mixing is exclusively contained within the expansion coefficients $a^{\nu l}_{mr}(k_{\|})$ [cf. Eq. (26)]. Consequently $I^{\nu}_{nrn'r'}(q)$ needs to be determined only once for each QW and can be used henceforth for any elevated stress value. Hence it is possible to obtain a complete excitonic absorption spectrum at finite uniaxial stress, which includes band mixing and stress-induced anisotropies, in fewer than 12 h on an ordinary PC. The calculations here were carried out using MATLAB for Windows on a 200 MHz Pentium PC with 128 MB of memory.[77]

III. EXPERIMENT

The sample was grown on a (100)-oriented GaAs substrate, and comprised GaAs and $Al_xGa_{1-x}As$ buffer layers, a ten-period multiple quantum well, with 100 Å GaAs wells and 500 Å $Al_{0.2}Ga_{0.8}As$ barriers, 1000 Å of $Al_{0.4}Ga_{0.6}As$, and finally 500 Å of GaAs. Uniaxial stress was applied with the cell previously used in Ref. 73. Polarized and unpolarized PR spectra were measured by phase-sensitive detection at temperatures between 20 and 80 K, using $\sim$5 W/cm^{-2} from a 670-nm diode laser to modulate the natural surface electric field in the sample (at $\sim$420 Hz). Two 0.3-m focal length monochromators were driven in tandem. The first ($M1$) dispersed the light from a 250 W tungsten lamp, which was then focused at an angle of incidence of 45° onto the sample so that it was coincident with the $\sim$2 mm^2 spot from the laser beam. The reflected light was collected at the entrance slit of the second monochromator ($M2$). A silicon detector was used at its exit slit. The slit widths of $M2$ were half those of $M1$, fixing the spectral resolution at $\sim$3 meV. Photoluminescence was also measured at 20 K, using 670-nm diode laser excitation.

A first derivative Lorenzian line shape (FDLL) formula was used to fit the experimental PR line shapes based on Eq. (13) of Ref. 74 with a dielectric function $\varepsilon = A + I/(E_{\rm ex} - E + i\Gamma)$, where E is the photon energy, A is a constant, I is related to the oscillator strength, $E_{\rm ex}$ is the exciton optical transition energy, and Γ is a broadening parameter. Assuming that oscillator strength modulation is negligible compared with energy and linewidth modulation,[74] the PR line shape for each exciton may be fitted to the formula

$$\frac{\Delta R}{R} \propto \left[\frac{\cos(\theta - 2\phi)}{(E_{\rm ex} - E)^2 + \Gamma^2} \right] \tag{30}$$

with fitting parameters $E_{\rm ex}$ and Γ, and where $\phi = \arctan[\Gamma/(E_{\rm ex} - E)]$. In spite of the additional complexity introduced into the line shape of the upper of the Fano doublets considered in this work,[75] the above fitting formula appeared to work very well, and was deemed adequate for estimating energies, linewidths, and relative intensities, which are the only data presented here in order to compare with calculation. Some of the measured spectra are presented in Ref. 13, but more detailed measurements and their analysis may be found elsewhere[76,77] and will be reported in a future publication.

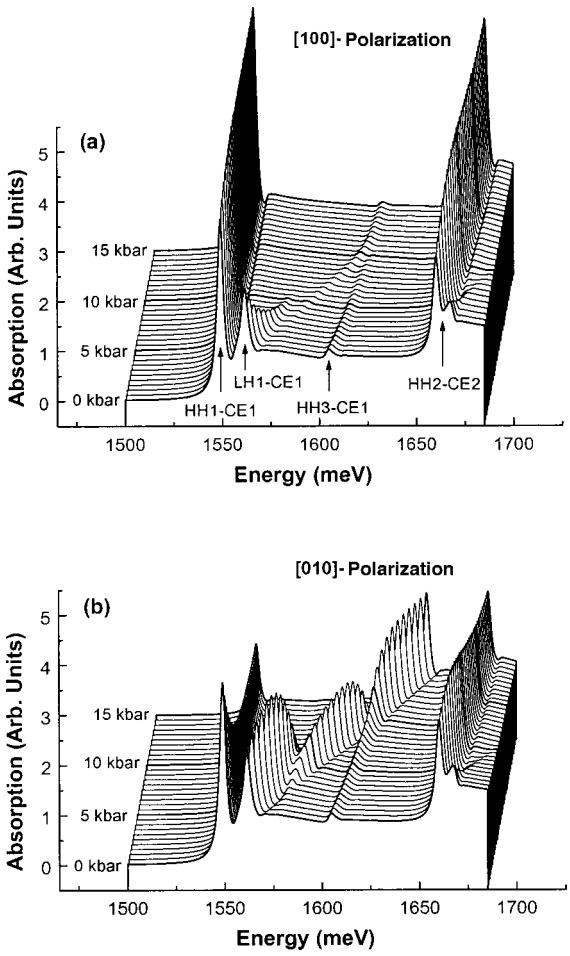

FIG. 3. Polarization dependence of the calculated excitonic absorption spectrum of a 100 Å $GaAs/Al_{0.3}Ga_{0.7}As$ QW for different values of in-plane uniaxial stress along the [100] direction.

IV. RESULTS AND DISCUSSIONS

Before we embark on a detailed discussion of the theoretical and experimental results, we would like to give a general overview of Fig. 3, which displays the evolution of the absorption spectrum of a 100 Å $GaAs/Al_{0.3}Ga_{0.7}As$ QW with respect to stress. The absorption spectrum is shown for two different in-plane polarization directions: (a) parallel to the stress direction and (b) perpendicular to the stress direction. Comparing these two polarization directions, it is evident at first sight that they yield very different results. While for [100] polarization the LH1-CE1($1s$) exciton practically disappears, it is strongly enhanced for [010] polarization. Conversely, the optically active HH excitons, i.e., HH1-CE1($1s$) and HH2-CE2($1s$), are enhanced for [100] polarization and attenuated for [010] polarization. Another feature that is also immediately apparent is the appearance of two anticrossings in the LH1-CE1($1s$) transition [cf. Fig. 3(b)]. The first anticrossing at about 4 kbar occurs when LH1-CE1($1s$) approaches the p continuum of HH2-CE1 and is due to the formation of Fano doublets, which we mentioned in the Introduction. The second anticrossing is a result of the stress-

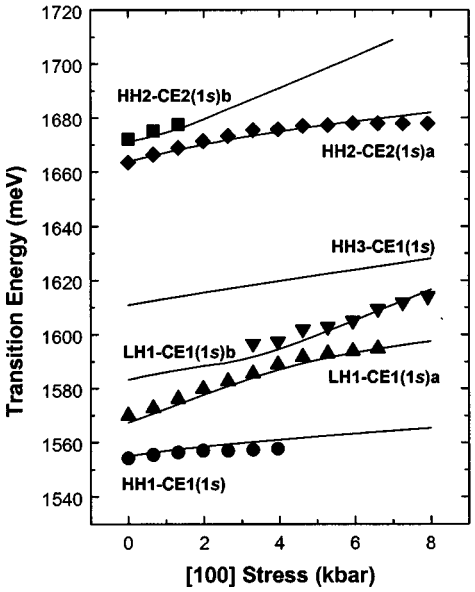

FIG. 4. Comparison between the experimental energy shifts of the lowest excitations (individual data points) in a 100 Å $GaAs/Al_{0.2}Ga_{0.8}As$ QW under in-plane uniaxial stress along the [100] direction, and the corresponding theoretical results (solid lines).

induced mixing between LH1 and HH3, which we discussed previously in Ref. 78 in the context of a simple single-particle zone-center model. The doublet structure of HH2-CE2(1*s*) at small stress values turns out to be an anticrossing as well, which can be explained by the same mechanism as the first anticrossing of LH1-CE1(1*s*). The main difference is that the anticrossing of HH2-CE2(1*s*) already occurs at zero stress.

A. Energy shifts and binding energies

We now present a more quantitative analysis of the various stress-induced features of the excitonic spectra. First we consider the energy shifts of the excitonic peaks found in the calculated absorption spectra of Fig. 3. These are shown in Fig. 4 as solid lines together with the experimental transition energies determined from our measured PR spectra. As can be clearly seen, the overall agreement between theory and experiment is excellent, which is quite remarkable given that the theoretical calculations are free of any adjustable parameter. The only slight discrepancy occurs for HH2-CE2(1*s*) at high stress and can be attributed to the omission of the spin-orbit coupling in our calculations. The experimental transition energies of HH1-CE1(1*s*) could be determined reliably only up to about 4 kbar, since at higher stress values the signal was clouded by the bulk GaAs HH-CE transition of the cap layer, which is shifted strongly by uniaxial stress to higher energies. Most importantly, however, the data reproduce the anticrossing of LH1-CE1(1*s*) at about 4 kbar very precisely including the minimum separation energy and thus provide conclusive evidence for the existence of Fano doublets.

Further insights into the stress effects on excitonic spectra can be gained from the stress dependence of the exciton binding energies. Here we determine the binding energies by

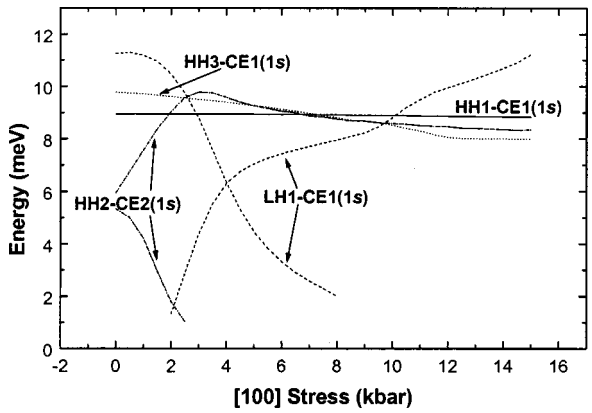

FIG. 5. Binding energies of the first four *s* excitons under compressive in-plane uniaxial stress along the [100] direction in a 100 Å $GaAs/Al_{0.3}Ga_{0.7}As$ QW determined from full band-mixing calculations including the stress-induced anisotropy.

simply taking the difference between the peak positions and the band edges of the corresponding single-particle transitions. The results are presented in Fig. 5. It is found that the binding energies of HH1-CE1(1*s*) and LH1-CE1(1*s*) at zero stress are 9.0 and 11.2 meV, respectively. This agrees well with numerical results that various groups obtained from variational calculations for similar systems,[3–6] whereas more recently published values tend to be slightly larger.[8,11,45,46] In the latter cases additional effects, which are neglected here, were included as well, such as nonparabolicity of the conduction band and difference in dielectric constants between well and barrier materials. As far as the stress dependence of the binding energies is concerned, HH1-CE1(1*s*) is essentially independent of stress, while the binding energies of all higher excited states exhibit a marked stress dependence. These changes in binding energies can be most conveniently understood in terms of stress-induced changes of the effective masses of the valence subbands. Thus the decrease of the HH3-CE1(1*s*) binding energy with increasing stress can be linked to a decrease of the effective mass. It was mentioned earlier that the HH3 subband is significantly modified by LH2 due to strong $\mathbf{k}\cdot\mathbf{p}$ coupling, because of which it assumes an electronlike band dispersion (cf. Fig. 1.). This yields a large reduced mass and accordingly a large binding energy for the exciton. As LH2 is shifted away from HH3, however, this effect weakens and consequently the binding energy gets smaller. An analogous argument, which is similarly based on electronlike subband dispersions, can be invoked to explain the characteristic stress dependence of the LH1-CE1(1*s*) and HH2-CE2(1*s*) binding energies. In both cases the binding energy has a maximum near the respective anticrossing. For LH1-CE1(1*s*) it occurs just before the anticrossing, while for HH2-CE2(1*s*) it occurs just afterwards, which follows directly from the opposite dispersions that LH1 and HH1 have near the zone center due to their mutual repulsion (cf. Fig. 1). This suggests that the enhanced binding energies near the anticrossings indeed also originate from the strong electronlike curvature of the corresponding hole subbands. An effective-mass argument would also explain why the binding energy of LH1-CE1(1*s*) is considerably smaller immediately after the anticrossing. Since LH1 and HH2 swap

their respective features as LH1 moves through HH2 (cf. Fig. 1), LH1 has a parabolic dispersion and hence a much smaller effective mass afterwards. Even though these arguments are quite plausible and in that sense satisfactory, it should be emphasized at this point that they are not rigorous. Their main shortcoming is that they cannot actually account for the occurrence of the two Fano-related anticrossings. The reason is that in the effective-mass picture the Coulomb potential is tacitly assumed to be constant, i.e., it is assumed not to be affected by the valence-band mixing. According to the discussion of the preceding section, this is clearly not the case in general, especially when LH1 and HH2 are in close proximity. Nevertheless, the effective-mass picture serves as a useful tool to interpret the complicated stress dependence of the exciton binding energies.

B. Anticrossings

In this subsection we will discuss in more detail the two types of anticrossings that can be observed in the absorption line of LH1-CE1($1s$) at elevated stress values. As was mentioned earlier, the first anticrossing occurs when LH1-CE1($1s$) approaches the onset of the HH2-CE1(p) continuum and can be best described within the framework of the Fano-Anderson model. In Ref. 12 we showed that in this particular case the Fano-Anderson model behaves like a two-state system, where one of the two states is a real state, i.e., LH1-CE1($1s$), while the other is an ''image'' state, comprising the collective effect of the HH2-CE1(p) continuum. Although we already gave an exhaustive account in Ref. 12 of the conditions for the formations of these Fano doublets, and of the characteristic features that distinguish them from conventional anticrossings, we discarded the effects of the stress-induced anisotropy for simplicity's sake. Hence the main focus here will be to investigate these Fano doublets under realistic conditions including the additional anisotropy.

One of the findings of our analysis in Ref. 12 was that the minimum separation energy ΔE of the Fano doublets during the anticrossing depends inversely on the width L of the QW, which in turn could be directly linked to the underlying valence-band mixing. In Fig. 6 we therefore compare the theoretical width dependence of ΔE for the two cases, i.e., when the stress-induced anisotropy is included (filled squares) and when it is neglected (open squares). As can be quite clearly seen, the minimum separation energies for these two cases are essentially identical over a wide range of QW widths. For very large QW widths, slight deviations occur, which are more likely connected to uncertainties in extracting ΔE from calculated absorption spectra than to any anisotropy effects. This means that the influence of the stress-induced anisotropy on the main features of the Fano doublets is negligible.

Besides the width dependence of ΔE, it is also interesting to look briefly at the width dependence of the anticrossing stress X, i.e., the stress at which the separation energy of the Fano doublet reaches its minimum. Results of the full-band-mixing model for X versus L are presented as filled circles in Fig. 6. Comparing $\Delta E(L)$ with $X(L)$ reveals a striking qualitative difference. Unlike $\Delta E(L)$, $X(L)$ changes much more abruptly from a gradual increase for large L to a steep increase for small L. This suggests that the functional dependence of $X(L)$ must be different from $\Delta E(L)$, which was found to be proportional to $1/(a_0 L)$, where a_0 is the Bohr radius of the pseudo-2D exciton. For a qualitative estimate of the L dependence of X, it is reasonable to assume that X is proportional to the zero stress energy difference between LH1-CE1($1s$) and its image state. Since the image state lies at the onset of the HH2-CE1(p) continuum, it is easy to show that

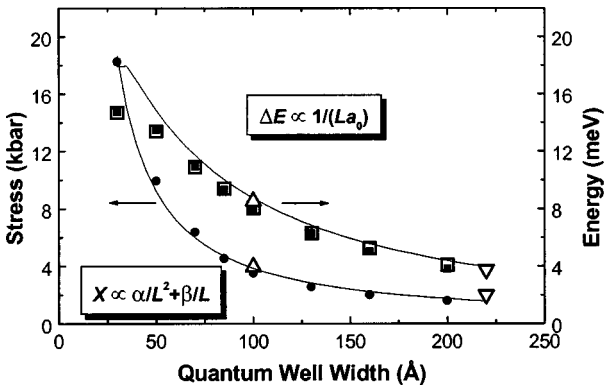

FIG. 6. Width dependence of the energy (squares) and the corresponding stress values (circles) of the anticrossing between LH1-CE1($1s$) and HH2-CE1(p). The filled/open squares represent the results of the full-band-mixing calculations including/excluding the stress-induced anisotropy while the solid lines represent simplified calculations using the Fano-Anderson model. The open upper triangles depict experimental results obtained from photoreflectance spectra of a 100 Å $GaAs/Al_{0.2}Ga_{0.8}As$ QW while the open lower triangles represent experimental results obtained from photoluminescence excitation spectra of a 220 Å $GaAs/Al_{0.3}Ga_{0.7}As$ QW (cf. Ref. 9).

$$X \propto E_0^{\mathrm{HH2}} - E_0^{\mathrm{LH1}} + E_b^{\mathrm{LH1}}, \tag{31}$$

where E_0^{HH2} and E_0^{LH1} refer to the confinement energies of HH2 and LH1, respectively, whereas E_b^{LH1} is the binding energy of LH1-CE1($1s$). While the width dependence of confinement energies in QW's is easily determined and approximately proportional to $1/L^2$, it is much less straightforward to find the right functional form for E_b^{LH1}. It turns out, however, that it is reasonable to assume an inverse relation between the binding energy and the QW width, at least for the range of L values that is of interest here. Thus Eq. (31) can be rewritten as follows:

$$X \propto \alpha/L^2 + \beta/L. \tag{32}$$

Equation (32) fits the values obtained from the full-band-mixing model very well, as can be seen in Fig. 6, which retrospectively justifies the assumption made about E_b^{LH1}. This explains now the qualitative difference between $\Delta E(L)$ and $X(L)$. While $\Delta E(L)$ always depends inversely on L, $X(L)$ depends on L as $1/L$ for large L and as $1/L^2$ for small L.

At this point it should also be mentioned that the good agreement in Fig. 6 could only be achieved because of the second term in Eq. (32). Assuming simply a $1/L^2$ dependence for X did not give good fits. The presence of the second term in Eq. (32) is a direct consequence of the peculiar

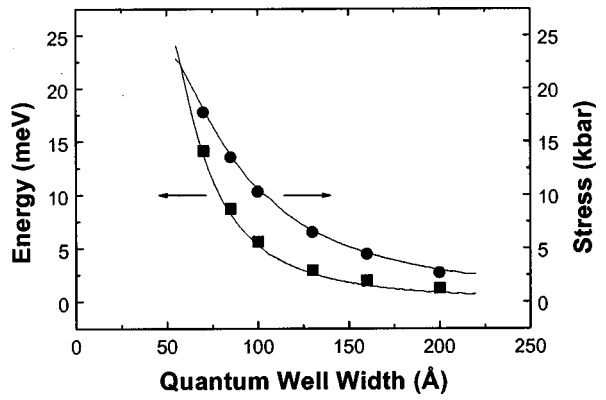

FIG. 7. Width dependence in a GaAs/$Al_{0.3}Ga_{0.7}As$ QW of the anticrossing energy separation (squares) between LH1 and HH3. The circles present the stress value at which the anticrossing occurs. The solid lines represent the corresponding single-particle results at the zone center.

properties of the image state, which is positioned at the band edge, not below it, and in that sense has no binding energy. If it did, it would approximately cancel E_b^{LH1} in Eq. (31) and thus remove the $1/L$ dependence in Eq. (32). Therefore, it is possible to say that the characteristic width dependence of X can be considered as a fingerprint of the unusual nature of the image state, just like the characteristic width dependence of ΔE turned out to be a fingerprint of the underlying valence-band mixing.

In Fig. 6 we also show experimental results comprising both anticrossing energy and anticrossing stress. The data for the 220 Å GaAs/$Al_{0.3}Ga_{0.7}As$ QW (downward triangle) were determined by Broido and Yang[9] from photoluminescence excitation data measured by Koteles *et al.*,[58] while the data for the 100 Å GaAs/$Al_{0.2}Ga_{0.8}As$ QW (upward triangle) were obtained by us from photoreflectance measurements. In both cases the theoretical predictions are seen to agree well with the experimental findings, confirming the high accuracy of our calculations.

The second anticrossing occurs when LH1-CE1($1s$) approaches HH3-CE1($1s$) and hence, unlike in the Fano doublet case, *two real* states interfere with each other. In Ref. 78 we showed that this anticrossing can already be accounted for within a simple single-particle picture. It can be ascribed to the finite size of the QW, since only in finite QW's can the HH3 and LH1 envelope functions have a finite overlap and hence be coupled by in-plane stress. When comparing the excitonic results for both anticrossing energy and anticrossing stress with the corresponding single-particle zone-center results in Fig. 7, it is found that they are practically identical. This is not surprising, since the stress Hamiltonian H^X does not depend on $k_\parallel$, so that the coupling matrix element between the two $1s$ states can be considerably simplified to

$$\langle \Psi^{1s}_{\text{LH1-CE1}} | H^X | \Psi^{1s}_{\text{HH3-CE1}} \rangle = \langle g_{\text{LH1}} | H^X | g_{\text{HH3}} \rangle \langle \phi^{1s}_{11} | \phi^{1s}_{13} \rangle, \tag{33}$$

where the first term on the right-hand side of Eq. (33) is just the respective single-particle coupling matrix element and $\langle \phi^{1s}_{11} | \phi^{1s}_{13} \rangle \approx 1$. Hence both excitonic and single-particle states are coupled by the same matrix element and consequently must reveal the same anticrossing behavior. At this point it is interesting to note that in agreement with the previous argument the anticrossing stress $X(L)$ depends on the QW width L approximately as $1/L^2$. Here both anticrossing states have proper binding energies, which are similar in size. Therefore, the zero stress energy separation of the two excitonic states is roughly equal to the zero stress separation of the respective zone-center states and thus $X \propto E_0^{\mathrm{HH3}} - E_0^{\mathrm{LH1}} \propto 1/L^2$. For the width dependence of the anticrossing energy $\Delta E(L)$, on the other hand, a similarly simple approximation cannot be derived. The reason is that $\Delta E(L)$ depends not only on $E_0^{\mathrm{HH3}} - E_0^{\mathrm{LH1}}$ but also on the overlap integral $r_{\mathrm{HH3,LH1}}$ between HH3 and LH1, whose width dependence cannot be determined analytically. The additional contribution of the overlap integral $r_{\mathrm{HH3,LH1}}$ to $\Delta E(L)$ explains, however, the qualitative difference between the width dependence of $X(L)$ and $\Delta E(L)$, which incidentally is just the opposite of what was found for Fano doublets in Fig. 6.

C. Oscillator strengths

Undoubtedly the most noticeable effect of the stress-induced anisotropy on the optical absorption spectra in Fig. 3 is the distinct dependence of the absorption on the polarization direction within the QW plane. To investigate this in more detail, we present in Figs. 8(a) and 8(b) the stress dependence of the oscillator strength of HH1-CE1($1s$) and LH1-CE1($1s$), respectively, for both [100] and [010] polarization. In each case three different models are compared with each other. The solid lines are the results obtained from the full-band-mixing model (FBM), which we introduced above, whereas the dashed lines represent simple zone-center results in the single-particle model (SPM). Finally, the dotted lines depict the results of a strongly simplified exciton model, which we henceforth will refer to as the ''image state model''(ISM). It only includes three discrete states, namely HH1-CE1($1s$), LH1-CE1($1s$), and the image state of LH1-CE1($1s$), which replaces the whole HH2-CE1(p) continuum to account for the effect of the $\mathbf{k}\cdot\mathbf{p}$ coupling between the HH2-CE1(p) continuum and LH1-CE1($1s$). The image state is located at the onset of the HH2-CE1(p) continuum and its wave function is optically inactive except for the admixture from the LH1-CE1($1s$) wave function.

For the two simplified models, the oscillator strength is straightforward to determine. For the FBM, on the other hand, it is more difficult, since higher excited exciton states are not properly bound stationary states, but have a finite lifetime due to Fano-Anderson-type interference. Thus they are broadened resonances and as such cannot be treated as single excitations anymore. For that reason we simply set the oscillator strength equal to the maximum transition intensity of the absorption peak minus the corresponding background. Even though this definition is not rigorous, it nevertheless provides at least a crude measure for the oscillator strength, which for our present purposes is adequate.

Comparing the three models now for the two different exciton transitions yields the following results. For the oscillator strength of HH1-CE1($1s$) shown in Fig. 8(a), all three different models are found to be in excellent agreement over the entire stress range and for both polarizations. For LH1-CE1($1s$) the situation is a bit more complicated. While all three models agree very well for the [100] polarization

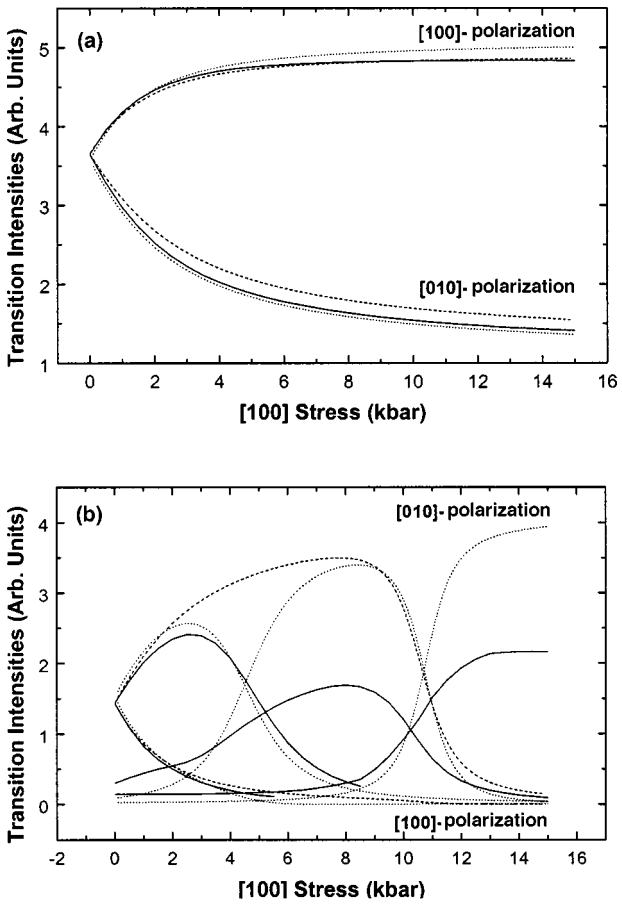

FIG. 8. Polarization dependence of the transition intensities of (a) HH1-CE1($1s$) and (b) LH1-CE1($1s$) in a 100 Å $GaAs/Al_{0.3}Ga_{0.7}As$ QW under in-plane uniaxial stress along the [100] direction. The solid lines are obtained from the full-band-mixing model. The dashed lines represent the corresponding oscillator strengths of the single-particle model, while the dotted lines show the results of the image-state model.

and hence uniformly predict the disappearance of the LH1-CE1($1s$) oscillator strength for this polarization direction, each model yields a slightly different result for the [010] polarization. The latter directly reflects the different levels of sophistication that the three models incorporate. The SPM only reproduces the general upward trend and the dip at about 10 kbar caused by the anticrossing with HH3-CE1($1s$), while the ISM also captures the second dip between 4 and 5 kbar due to the anticrossing between LH1-CE1($1s$) and its image state. Neither of these simplified models, however, can account for the much smaller overall oscillator strength obtained from the FBM. This is to be expected, since the reduced oscillator strength is a direct consequence of Fano-Anderson-related broadening, which is not included in the simple models.

It can therefore be said that the polarization dependence of excitonic states in QW's at elevated stress can be adequately described by a simple single-particle model, which only comprises the corresponding zone-center states. All extra features in the stress dependence of the oscillator strengths, which cannot be reproduced by the SPM, are *not* caused by the stress-induced symmetry reduction but by excitonic mixing effects. In the simple single-particle zone-center model, however, the change of the oscillator strength for the various hole states can be easily explained, since it is directly linked to the stress-induced mixing of the Bloch functions. As we discussed in Ref. 78, in-plane uniaxial stress rotates the natural quantization direction in a QW by 90° from the confinement direction at low stress values to the stress direction at large stress values. At the same time, a HH-type Bloch function turns into a LH-type Bloch function and vice versa. If the new quantization direction at large stress values is chosen as the new z axis, the oscillator strengths for the two in-plane directions of the QW, i.e., [100] and [010], effectively become identical to the corresponding ones in bulk for the z and y direction, respectively.

With this mechanism in mind, it becomes straightforward to interpret the results shown in Fig. 8. For small and large stress values the oscillator strengths equal to the corresponding bulk oscillator strengths, which are found to be directly related to the Clebsch-Gordan coefficients of the Bloch function. Thus the oscillator strength for HH1-CE1 in Fig. 8(a) at zero stress is $\frac{1}{2}$ for both directions, which corresponds to the bulk HH oscillator strength along the x and y direction. At large stress values, on the other hand, it is $\frac{2}{3}$ for [100] and $\frac{1}{6}$ for [010] directions, which corresponds to the bulk LH oscillator strength along the z and y direction, respectively. For the LH1-CE1 transition shown in Fig. 8(b), the interpretation is analogous except that now a LH-type Bloch function turns into a HH-type Bloch function.

Finally, Figs. 9(a) and 9(b) present our experimental results for the transition intensities of HH1-CE1($1s$) and LH1-CE1($1s$), respectively. In both figures, squares refer to [100] polarization, i.e., parallel to the stress direction, and circles refer to [010] polarization, i.e., perpendicular to the stress direction. The data in Fig. 9(a) were obtained from PL measurements, while the data in Fig. 9(b) were obtained from PR measurements. Overall the transition intensities are seen to be in good agreement with the corresponding theoretical results (solid lines). Contrary to the PL data in Fig. 9(a), however, the PR data in Fig. 9(b) exhibit strong fluctuations and in parts noticeable deviations from the theoretical lines. The reason for this lies mainly in the difficulty of extracting precise intensity values from the complicated PR line shapes by merely fitting them with simple phenomenological fitting formulas that depend only on a few parameters. Nevertheless, all essential aspects of the previous theoretical discussion are confirmed by the experimental results. Most importantly, the nontrivial variation of the LH1-CE1($1s$) transition intensity for [010]-polarization near the anticrossing at about 4 kbar is clearly visible in Fig. 9(b). It is interesting to note that, in accordance with theory, the point of equal transition intensities (the ''optical'' anticrossing point) occurs at 5 kbar, i.e., at a higher stress value than the point of minimum anticrossing energy (the ''real'' anticrossing point). This is in contrast to an ordinary two-state system, where these two points coincide. This feature can be traced back to the strong broadening of the second peak in a Fano doublet compared with the first peak. The difference in broadening is clearly resolved in the experimental data, where the broadening of LH1-CE1($1s$) before and after the anticrossing is 4 and 5 meV, respectively. Detecting this subtle feature in the experimental spectra, therefore, provides further evidence for the existence of Fano doublets in the present system.

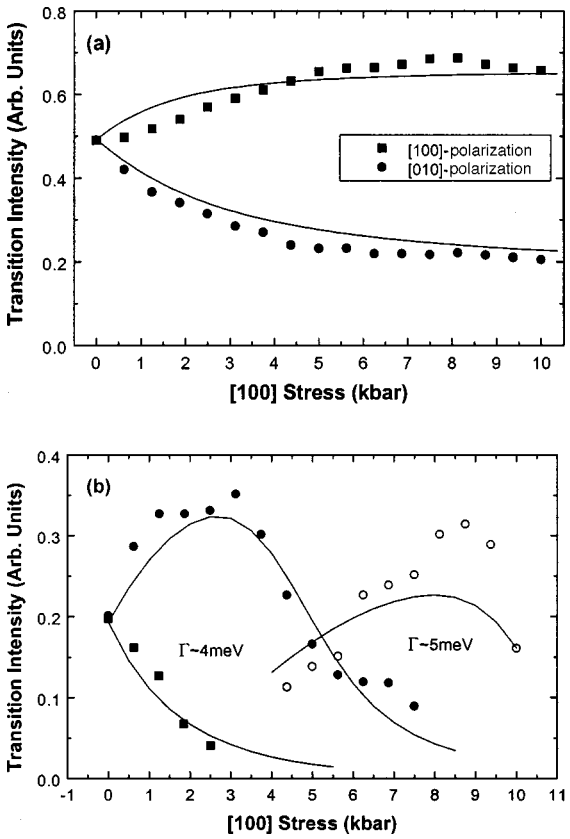

FIG. 9. Polarization dependence of the intensity of (a) HH1-CE1(1*s*) and (b) LH1-CE1(1*s*) in a 100 Å $GaAs/Al_{0.2}Ga_{0.8}As$ QW under in-plane uniaxial stress along the [100] direction. The individual data points in (a) and (b) are experimental results obtained from photoluminescence and photoreflectance spectra, respectively, and the solid lines are the corresponding theoretical results. Squares refer to [100] polarization while circles refer to [010] polarization.

V. CONCLUSION

We have studied, both theoretically and experimentally, the effects of large in-plane uniaxial stress on the optical properties of $GaAs/Al_xGa_{1-x}As$ QW's. In particular, we have investigated in great detail the mixing between excitonic states caused by valence-band mixing and have analyzed how this mixing is modified by stress. The analysis showed that stress is a powerful tool to reveal some of the striking optical features caused by exciton mixing. Specifically, the two main contributions of this work are (a) the development of a full-band-mixing model that goes beyond the axial approximation and hence allows the stress-induced *anisotropy* of the valence-subband structure to be taken into account, and (b) the characterization of the various mixing *mechanisms* that are intrinsic to quasi-two-dimensional systems under stress.

The main point about the extended full-band-mixing model was that the stress-induced anisotropy of the valence-subband structure can be described accurately by Fourier expanding the valence states only up to the first nonisotropic order. In the excitonic picture this means that each of the four total angular momenta that give finite contributions to the excitonic oscillator strength couples strongly only to *one* other total angular momentum under in-plane uniaxial stress. The coupling to angular momenta outside the subspace spanned by those four total angular momenta can be neglected. Consequently, the Hilbert space of the anisotropic case is only twice the size of the isotropic case, which numerically is still tractable.

When investigating the effects of valence-band mixing on the excitonic spectrum, it is important to distinguish carefully between mixing that is intrinsic to stress and mixing that is intrinsic to $\mathbf{k}\cdot\mathbf{p}$ coupling. Stress-induced mixing has a straightforward mechanism that can be understood within the framework of a simple single-particle zone-center model. The main aspect about in-plane uniaxial stress is that it rotates the natural quantization direction from the confinement direction to the stress direction, which leads to polarization-dependent absorption spectra and to the anticrossings between HH and LH states with the same parity, such as HH3 and LH1. Thus, on its own stress has no significant direct influence on excitonic quantities. Mixing effects caused by $\mathbf{k}\cdot\mathbf{p}$ coupling, on the other hand, are best explained within the excitonic picture. In this context, stress can be used to tune the relative strength of the various $\mathbf{k}\cdot\mathbf{p}$ coupling terms. This decisively modifies the binding energies of the higher excited states due to the stress-induced changes of the valence-band effective masses. Furthermore, it leads to a strong anticrossing feature between the discrete LH1-CE1(1*s*) and the *p* continuum of HH2-CE1, which can be best explained within the framework of the Fano-Anderson model. The characteristic width dependence of the stress value at which the double peak structure of the anticrossing reaches its minimum separation energy directly reflects the peculiar properties of Fano doublets.

The validity of our theoretical results was confirmed by a detailed analysis of experimental data, which we obtained from photoreflectance and photoluminescence measurements on a 100 Å $GaAs/Al_{0.2}Ga_{0.8}As$ QW. Excellent agreement between theory and experiment was achieved for both the stress dependence of the exciton energies and the polarization dependence of the transition intensities. This powerfully demonstrates the high accuracy of the theoretical results and unambiguously confirms the existence of Fano doublets.

ACKNOWLEDGMENTS

We would like to thank Nikos Nicopoulos for stimulating discussions and suggestions. This work was supported by the Engineering and Physical Sciences Research Council (EPSRC) of the U.K. and the Human Capital and Mobility program of the E.U. In particular, N.F.J. acknowledges the support of an EPSRC grant on Photonic Materials, P.C.K. acknowledges an E. U. Network grant (Grant No. CHRXCT930321), and A.R.G. acknowledges support from EPSRC and the Toshiba, Cambridge, Research Center. G.R. would like to thank the Harmsworth Trust of Merton College for its generous support.

APPENDIX: NUMERICAL SOLUTION

In this appendix we present our theoretical method for obtaining numerical solutions of the exciton equation [cf. Eq. (17)]. The solution technique is similar to the approach in Ref. 10 and is based on the Gaussian quadrature method. The

essence of this method is to approximate the integral by a finite sum of the following form:

$$\int_a^b f(x)dx \approx \sum_{j=1}^{N} w_j f(x_j), \tag{A1}$$

where x_j are the roots of appropriately chosen orthogonal polynomials of degree N and w_j are the corresponding weighting factors.[79] In order to turn the improper integral in Eq. (17) into a proper integral, we use the following coordinate transformation:

$$k = \frac{1}{2}\{-2k_0 \cot(\pi x) + k_1 x + \sqrt{[2k_0 \cot(\pi x) + k_1 x]^2 + 4\langle k\rangle_{1s}^2}\}, \tag{A2}$$

where

$$k_0 = \frac{k_T}{\tan\left(x_T \frac{\pi}{2}\right)}, \quad k_1 = \frac{k_T}{x_T}, \tag{A3}$$

and x runs from 0 to 1. Here k_T and x_T are adjustable parameters that are used to optimize the accuracy of the numerical results. What makes Eq. (A2) a particularly suitable coordinate transformation is that it increases linearly up to x_T, where k assumes the value k_T, and only then starts diverging to infinity. This means that Eq. (A2) permits control of the turning point between small k values near the origin and large k values. Hence with Eq. (A2) it is possible to set the percentage of the total number of k values that are smaller than $\langle k\rangle_{1s}$ exactly to the appropriate level, where $\langle k\rangle_{1s}$ refers to the momentum expectation value of the excitonic ground state.

Before we proceed to present the discretized form of the exciton equation (17), a few definitions are necessary. First, the modified weighting factor is defined as

$$W_i = \frac{k(x_i)}{2\pi}\left(\frac{dk}{dx}\right)_i w_i, \tag{A4}$$

where $(dk/dx)_i$ represents the Jacobian of the coordinate transformation (A2) at the point x_i. Furthermore, it is convenient to introduce

$$\tilde{\phi}_{nmi}^{Xs} = \sqrt{W_i}\,\phi_{nm}^{Xs}(k_i), \tag{A5}$$

$$T_{nmi}^{s-s'} = T_{nm}^{s-s'}(k_i), \tag{A6}$$

$$\tilde{V}_{nmin'm'j}^{ss'} = \sqrt{W_i} V_{nmn'm'}^{ss'}(k_i,k_j)\sqrt{W_j}. \tag{A7}$$

After these preliminaries it is straightforward to show that the discretized from of Eq. (17) can be written as follows:

$$\sum_{n',m'} \sum_{s'=\sigma-1/2}^{\sigma+3/2} \sum_{j=1}^{N} A_{nmin'm'j}^{ss'} \tilde{\phi}_{n'm'j}^{Xs'} = E_X \tilde{\phi}_{nmi}^{Xs}, \tag{A8}$$

where $A_{nmin'm'j}^{ss'}$ is a Hermitian matrix of the following form:

$$A_{nmin'm'j}^{ss'} = T_{nmi}^{s-s'} \delta_{nn'}\delta_{mm'}\delta_{ij} + \tilde{V}_{nmin'm'j}^{ss'}. \tag{A9}$$

Finally, we deal with the singularity of the Coulomb potential. It can be readily seen from the expression of Eq. (21) that the Coulomb matrix element $V_{nmn'm'}^{ss'}(k,k')$ scales like $1/q$ for small values of q, so that the validity of the quadrature method becomes questionable at $k_i = k_j$. Fortunately this difficulty can be circumvented, since the singularity of the Coulomb potential is integrable. Numerically this can be achieved by the so-called ''modified quadrature method.'' In the modified quadrature method the Coulomb matrix element $V_{nmn'm'}^{ss'}(k,k')$ in Eq. (17) is replaced near the singularity by a simplified expression $\Lambda_{nmn'm'}^{ss'}(k,k')$, which has the same type of singularity as $V_{nmn'm'}^{ss'}(k,k')$ but which can be integrated *exactly* across the singularity. Following Chao and Chuang[10] we choose the following form for $\Lambda_{nmn'm'}^{ss'}(k,k')$:

$$\Lambda_{nmn'm'}^{ss'}(k,k') = -\frac{e^2}{2\varepsilon\varepsilon_0}\frac{2k^2}{k^2+k'^2} \times \sum_{\nu} \sum_{l=0,\pm 2} \int_0^{2\pi} \frac{d\Delta\theta}{2\pi}\frac{1}{q}\cos(\mu\Delta\theta) \times \delta_{nn'} \int dz_h g_{m\nu}^{l}(k,z_h) g_{m'\nu}^{l-(s-s')*}(k,z_h). \tag{A10}$$

Here $\mu = \sigma - \nu - (s-l)$, while $2k^2/(k^2+k'^2)$ is a weighting function that is added to improve numerical convergence. Furthermore, the integral over the conduction-subband envelope functions disappears, because conduction-band mixing is neglected in this work. Consequently all conduction states are orthonormal at each k value. In the derivation by Chao and Chuang, the integral over the hole envelope functions was also set equal to $\delta_{mm'}$. This, however, is not correct in general, especially in the case of strong valence-band mixing, and hence this approximation is not adopted here. Finally, it is now possible with the help of Eq. (A10) to approximate $\tilde{V}_{nmn'm'}^{ss'}(k_i,k_i)$ as follows:

$$\tilde{V}_{nmn'm'}^{ss'}(k_i,k_i) \approx \int_{1/2(k_{i-1}+k_i)}^{1/2(k_i+k_{i+1})} \frac{k'dk'}{2\pi} V_{nmn'm'}^{ss'}(k_i,k') \approx \int_0^{\infty} \frac{k'dk'}{2\pi} \Lambda_{nmn'm'}^{ss'}(k_i,k') - \sum_{j\neq i}^{N} W_j \Lambda_{nmn'm'}^{ss'}(k_i,k_j). \tag{A11}$$

The crucial point about this approximation is that the sum in the second term only contains summands for which the quadrature method is valid, while the integral in the first term can be carried out exactly and has the following result:

$$\int_0^{\infty} \frac{k'dk'}{2\pi} \Lambda_{nmn'm'}^{ss'}(k_i,k') = -\frac{e^2}{8\pi\varepsilon\varepsilon_0} k_i \sum_{\nu} \sum_{l=0,\pm 2} \times C_{\mu}\delta_{nn'} G_{mm'\nu}^{l[l-(s-s')]}(k_i), \tag{A12}$$

where

$$G_{mm'\nu}^{l[l-(s-s')]}(k_i)=\int dz_h g_{m\nu}^{l}(k_i,z_h)g_{m'\nu}^{l-(s-s')*}(k_i,z_h), \tag{A13}$$

and

$$C_\mu=4\int_0^{2\pi}\frac{d\Delta\theta}{2\pi}\int_0^\infty dx\,\frac{x}{1+x^2}\,\frac{\cos(\mu\Delta\theta)}{\sqrt{x^2-2x\cos\Delta\theta+1}}. \tag{A14}$$

The double integral in Eq. (A14) is a standard integral that is well defined over the entire integration range and hence can be solved numerically to any degree of accuracy. It is easy to convince oneself that within the subspace spanned by the four total angular momenta $s=\sigma-\frac{3}{2}$, $\sigma-\frac{1}{2}$, $\sigma+\frac{1}{2}$, and $\sigma+\frac{3}{2}$, six different C_μ's are needed, i.e.,

$$C_0=5.2442,\quad C_2=0.918\,63,\quad C_4=0.486\,69,$$
$$C_1=1.6037,\quad C_3=0.637\,77,\quad C_5=0.392\,84. \tag{A15}$$

Under the axial approximation, on the other hand, only the first four values are needed.

[1] D. A. Broido and L. J. Sham, Phys. Rev. B **34**, 3917 (1986).
[2] B. F. Zhu and K. Huang, Phys. Rev. B **36**, 8102 (1987).
[3] K. S. Chan, J. Phys. C **19**, L125 (1986).
[4] U. Ekenberg and M. Altarelli, Phys. Rev. B **35**, 7585 (1987).
[5] U. Ekenberg and M. Altarelli, Superlattices Microstruct. **3**, 199 (1987).
[6] L. C. Andreani and A. Pasquarello, Europhys. Lett. **6**, 259 (1988).
[7] G. E. W. Bauer and T. Ando, Phys. Rev. B **38**, 6015 (1988).
[8] L. C. Andreani and A. Pasquarello, Superlattices Microstruct. **5**, 59 (1989).
[9] D. A. Broido and S. R. E. Yang, Phys. Rev. B **42**, 11 051 (1990).
[10] C. Y. P. Chao and S. L. Chuang, Phys. Rev. B **48**, 8210 (1993).
[11] R. Winkler, Phys. Rev. B **51**, 14 395 (1995).
[12] G. Rau, P. C. Klipstein, and N. F. Johnson, Phys. Rev. B **58**, 7210 (1998).
[13] A. R. Glanfield, G. Rau, P. C. Klipstein, and G. W. Smith, in 8th International Conference on High Pressure Semiconductor Physics [Phys. Status Solidi B **211**, 269 (1999)].
[14] D. A. B. Miller, D. S. Chemla, T. C. Damen, A. C. Gossard, W. Wiegman, T. H. Wood, and C. A. Burrus, Phys. Rev. Lett. **53**, 2173 (1984).
[15] R. T. Collins, L. Viña, W. I. Wang, L. L. Chang, L. Esaki, K. Vonklitzing, and K. Ploog, Phys. Rev. B **36**, 1531 (1987).
[16] L. Viña, R. T. Collins, E. E. Mendez, and W. I. Wang, Phys. Rev. Lett. **58**, 832 (1987).
[17] P. W. Yu, G. D. Sanders, K. R. Evans, D. C. Reynolds, K. K. Bajaj, C. E. Stutz, and R. L. Jones, Phys. Rev. B **38**, 7796 (1988).
[18] G. D. Sanders and K. K. Bajaj, Phys. Rev. B **35**, 2308 (1987).
[19] D. A. Broido, Superlattices Microstruct. **3**, 13 (1987).
[20] G. E. W. Bauer and T. Ando, J. Phys. (Paris) **48**, 215 (1987).
[21] B. Zhu, Phys. Rev. B **38**, 13 316 (1988).
[22] D. M. Whittaker, Superlattices Microstruct. **7**, 375 (1990).
[23] S. L. Chuang, S. Schmitt-Rink, D. A. B. Miller, and D. S. Chemla, Phys. Rev. B **43**, 1500 (1991).
[24] G. Z. Wen and Y. C. Chang, Phys. Rev. B **45**, 6101 (1992).
[25] D. W. Peggs, M. S. Skolnick, D. M. Whittaker, R. A. Hogg, A. R. K. Willcox, D. J. Mowbray, R. Grey, G. J. Rees, L. Hart, M. Hopkinson, G. Hill, and M. A. Pate, Phys. Rev. B **52**, 14 340 (1995).
[26] R. C. Miller, D. A. Kleinman, W. T. Tsang, and A. C. Gossard, Phys. Rev. B **24**, 1134 (1981).
[27] G. Bastard, E. E. Mendez, L. L. Chang, and L. Esaki, Phys. Rev. B **26**, 1974 (1982).
[28] R. L. Greene, K. K. Bajaj, and D. E. Phelps, Phys. Rev. B **29**, 1807 (1984).
[29] D. A. B. Miller, D. S. Chemla, T. C. Damen, A. C. Gossard, W. Wiegman, T. H. Wood, and C. A. Burrus, Phys. Rev. B **32**, 1043 (1985).
[30] W. T. Masselink, P. J. Pearah, J. Klem, C. K. Peng, H. Morkoç, G. D. Sanders, and Y. C. Chang, Phys. Rev. B **32**, 8027 (1985).
[31] G. D. Sanders and Y. C. Chang, Phys. Rev. B **31**, 6892 (1985).
[32] G. D. Sanders and Y. C. Chang, Phys. Rev. B **32**, 4282 (1985).
[33] G. D. Sanders and Y. C. Chang, Phys. Rev. B **32**, 5517 (1985).
[34] G. D. Sanders and Y. C. Chang, Phys. Rev. B **35**, 1300 (1987).
[35] H. Chu, G. D. Sanders, and Y. C. Chang, Phys. Rev. B **36**, 7955 (1987).
[36] T. Hiroshima, Phys. Rev. B **36**, 4518 (1987).
[37] G. E. W. Bauer and T. Ando, Phys. Rev. Lett. **59**, 601 (1987).
[38] K. S. Chan, J. Phys. C **20**, 791 (1987).
[39] B. F. Zhu, Phys. Rev. B **37**, 4689 (1988).
[40] J. Lee, M. O. Vassell, E. S. Koteles, and B. Elman, Phys. Rev. B **39**, 10 133 (1989).
[41] J. Lee, M. O. Vassell, E. S. Koteles, C. Jagannath, K. T. Hsu, G. J. Jan, C. P. Liu, and I. F. Chang, Phys. Rev. B **40**, 1703 (1989).
[42] J. P. Loehr and J. Singh, Phys. Rev. B **42**, 7154 (1990).
[43] C. Y. P. Chao and S. L. Chuang, Phys. Rev. B **43**, 6530 (1991).
[44] A. Pasquarello, L. C. Andreani, and R. Buczko, Phys. Rev. B **40**, 5602 (1989).
[45] L. C. Andreani and A. Pasquarello, Phys. Rev. B **42**, 8928 (1990).
[46] L. C. Andreani and A. Pasquarello, Superlattices Microstruct. **9**, 1 (1991).
[47] R. P. Leavitt and J. W. Little, Phys. Rev. B **42**, 11 774 (1990).
[48] H. Chu and Y. C. Chang, Phys. Rev. B **36**, 2946 (1987).
[49] H. Y. Chu and Y. C. Chang, Phys. Rev. B **39**, 10 861 (1989).
[50] M. W. Berz, L. C. Andreani, E. F. Steigmeier, and F. K. Reinhart, Solid State Commun. **80**, 553 (1991).
[51] P. M. Young, H. Ehrenreich, P. M. Hui, and N. F. Johnson, J. Appl. Phys. **74**, 7369 (1993).
[52] R. Andre, J. Cibert, and L. S. Dang, Phys. Rev. B **52**, 12 013 (1995).
[53] P. Harrison, T. Piorek, W. E. Hagston, and T. Stirner, Superlattices Microstruct. **20**, 45 (1996).
[54] G. Debarge, D. Erasme, and A. Toledoalvarez, Phys. Rev. B **53**, 3983 (1996).
[55] S. Glutsch, D. S. Chemla, and F. Bechstedt, Phys. Rev. B **54**, 11 592 (1996).
[56] R. C. Iotti and L. C. Andreani, Phys. Rev. B **56**, 3922 (1997).
[57] N. Linder, Phys. Rev. B **55**, 13 664 (1997).

[58] E. S. Koteles, C. Jagannath, J. Lee, Y. J. Chen, B. S. Elman, and J. Y. Chi, in *18th International Conference on the Physics of Semiconductors*, edited by O. Engstrom (World Scientific, Singapore, 1987), p. 625.
[59] C. Jagannath, E. S. Koteles, J. Lee, Y. J. Chen, B. S. Elman, and J. Y. Chi, Phys. Rev. B **34**, 7027 (1986).
[60] R. Sooryakumar, A. Pinczuk, A. C. Gossard, D. S. Chemla, and L. J. Sham, Phys. Rev. Lett. **58**, 1150 (1987).
[61] J. Lee, C. Jagannath, M. O. Vassell, and E. S. Koteles, Phys. Rev. B **37**, 4164 (1988).
[62] B. Gil, P. Lefebvre, H. Mathieu, G. Platero, M. Altarelli, T. Fukunaga, and H. Nakashima, Phys. Rev. B **38**, 1215 (1988).
[63] S. S. Lu, K. R. Lee, K. H. Lee, M. I. Nathan, M. Heiblum, and S. L. Wright, J. Appl. Phys. **67**, 6360 (1990).
[64] S. S. Lu, C. C. Meng, F. Williamson, and M. I. Nathan, J. Appl. Phys. **69**, 8241 (1991).
[65] P. Boring, J. M. Jancu, B. Gil, D. Bertho, C. Jouanin, and K. J. Moore, Phys. Rev. B **46**, 4764 (1992).
[66] P. Boring, B. Gil, and K. J. Moore, Phys. Rev. B **45**, 8413 (1992).
[67] D. A. Broido and L. J. Sham, Phys. Rev. B **31**, 888 (1985).
[68] Because of the strong mixing between the different subbands away from the zone center, it is strictly speaking not possible to ascribe a particular hole type to any subband. It is customary, however, to use the well defined hole state at the zone center as a label for the entire subband. This convention will be adopted throughout this work.
[69] E. P. O'Reilly and G. P. Witchlow, Phys. Rev. B **34**, 6030 (1986).
[70] E. P. O'Reilly, Semicond. Sci. Technol. **4**, 121 (1989).
[71] J. Lee and M. O. Vassell, Phys. Rev. B **37**, 8861 (1988).
[72] L. J. Sham and T. M. Rice, Phys. Rev. **144**, 708 (1966).
[73] W. R. Tribe, P. C. Klipstein, G. W. Smith, and R. Grey, Phys. Rev. B **54**, 8721 (1996).
[74] A. J. Shields and P. C. Klipstein, Phys. Rev. B **43**, 9118 (1991).
[75] G. Rau, P. C. Klipstein, A. R. Glanfield, and N. F. Johnson, in *24th International Conference on the Physics of Semiconductors*, edited by E. Cohen (World Scientific, Singapore, 1999).
[76] A. R. Glanfield, Ph.D. thesis, University of Oxford, Oxford (1998).
[77] G. Rau, Ph.D. thesis, University of Oxford, Oxford (1998).
[78] G. Rau, P. C. Klipstein, V. N. Nicopoulos, and N. F. Johnson, Phys. Rev. B **54**, 5700 (1996).
[79] G. Arfken, *Mathematical Methods for Physicists* (Academic, London, 1985).